Article

Low-Temperature Propane Activation and Mineralization over a Co$_3$O$_4$ Sub-nanometer Porous Sheet: Atomic-Level Insights

Yanfei Jian, Zeyu Jiang, Mingjiao Tian, Mudi Ma, Lianghui Xia, Shouning Chai, Jingjing Wang, Reem Albilali, and Chi He*

Read Online

ACCESS | Metrics & More | Article Recommendations | Supporting Information

ABSTRACT: Light alkanes make up a class of widespread volatile organic compounds (VOCs), bringing great environmental hazards and health concerns. However, the low-temperature catalytic destruction of light alkanes is still a great challenge to settle due to their high reaction inertness and weak polarity. Herein, a Co$_3$O$_4$ sub-nanometer porous sheet (Co$_3$O$_4$-SPS) was fabricated and comprehensively compared with its bulk counterparts in the catalytic oxidation of C$_3$H$_8$. Results demonstrated that abundant low-coordinated Co atoms on the Co$_3$O$_4$-SPS surface boost the activation of adsorbed oxygen and enhance the catalytic activity. Moreover, Co$_3$O$_4$-SPS has better surface metal properties, which is beneficial to electron transfer between the catalyst surface and the reactant molecules, promoting the interaction between C$_3$H$_8$ molecules and dissociated O atoms and facilitating the activation of C−H bonds. Due to these, Co$_3$O$_4$-SPS harvests a prominent performance for C$_3$H$_8$ destruction, 100% of which decomposed at 165 °C (apparent activation energy of 49.4 kJ mol^{-1}), much better than the bulk Co$_3$O$_4$ (450 °C and 126.9 kJ mol^{-1}) and typical noble metal catalysts. Moreover, Co$_3$O$_4$-SPS also has excellent thermal stability and water resistance. This study deepens the atomic-level insights into the catalytic capacity of Co$_3$O$_4$-SPS in light alkane purification and provides references for designing efficacious catalysts for thermocatalytic oxidation reactions.

KEYWORDS: Co$_3$O$_4$, atomic thickness, propane, catalytic oxidation, DFT study
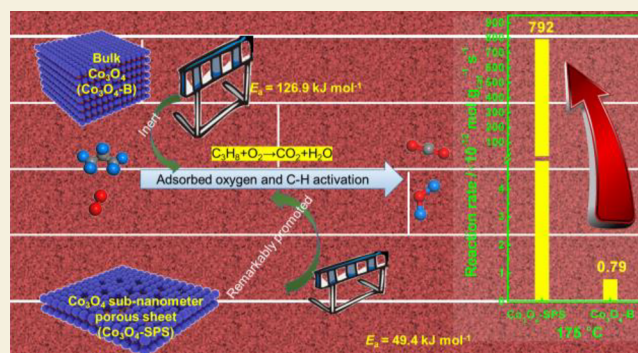
1. INTRODUCTION

The emission of industrial volatile organic compounds (VOCs) can cause serious environment hazards,[1−6] and efficient VOC elimination has become one of the most critical issues to be solved. Among them, light alkanes such as propane (C$_3$H$_8$) are a class of widespread and intractable pollutants due to their stable molecular structures.[7] Although previous research has shown that some precious metal-loaded materials such as Pt/ZSM-5,[8] Pd/TiO$_2$,[9] and Pd/WO$_x$/TiO$_2$[9] show superior activity in catalytic oxidation of C$_3$H$_8$, their high cost and easy inactivation at high temperatures limit their applications. In comparison, the transition metal oxides which have low cost, considerably activity and excellent thermal stability have received great attention.[10,11] For example, in the lattice of Co$_3$O$_4$ spinel oxide, the 16 octahedral and eight tetrahedral sites are occupied by Co^{3+} and Co^{2+} cations respectively that has a relatively high catalytic activity owing to low reaction enthalpies (ΔH) for O$_2$ vaporization. In general, the Co−O bond strength of Co$_3$O$_4$ can affect the ease of dissociation of lattice oxygen.[12] Many previous works describe how to increase the activity of cobalt oxide by exposing more reactive crystal faces or adjusting the morphology.[13−15] Xie et al.[13] have shown that CO can be

completely oxidized at −77 °C by Co$_3$O$_4$ nanroad which mainly exposed (110) crystal plane. They pointed out that the high catalytic activity is mainly attributed to abundant Co^{3+} in the (110) plane. Tang et al.[10] proposed that porous Co$_3$O$_4$ nanoparticles can oxidized 90% propane under a w8 hly space velocity of 240,000 mL g^{-1} h^{-1} at 250 °C, even better than the commercial Pt/Al$_2$O$_3$ and Pt/CeO$_2$ catalysts. However, the performance of Co$_3$O$_4$ materials in catalytic low-temperature destruction of light alkanes is still far from satisfactory.[16,17]

Two-dimensional (2D) nanomaterials have a large area-to-thickness aspect ratios mainly due to their sheet-like nanostructures with thicknesses ranging from a single layer to several unit cells.[18,19] The geometric constraints in the third dimension of space may cause their physical and chemical properties to be significantly different from those of their bulk counterparts. This structure has an impact on quantum
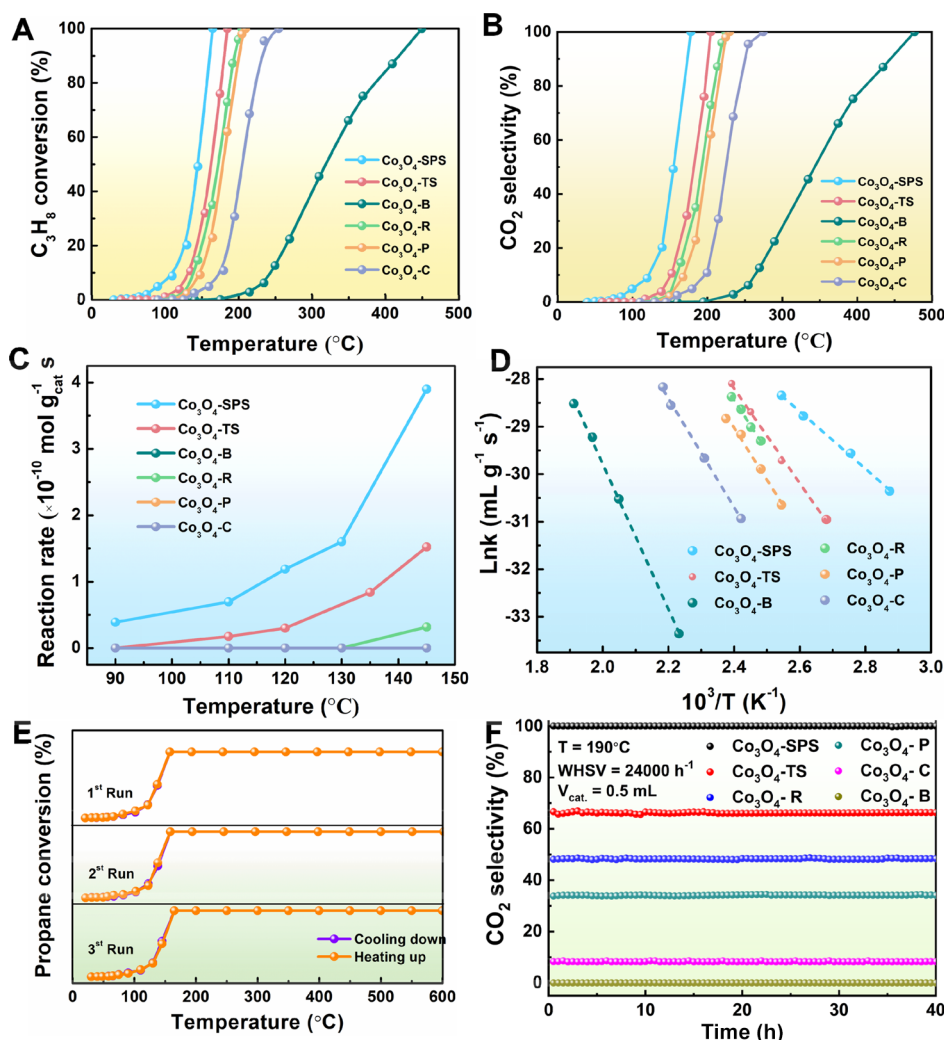
Figure 1. Catalytic performance of prepared catalysts: (A) catalytic activity, (B) CO_2 selectivity, (C) reaction rate, (D) corresponding Arrhenius plots; (E) stability tests of Co_3O_4-SPS from 40 to 600 °C; (F) time-on-stream stability of CO_2 yield.

confinement. In addition, the large surface area and high concentration of surface defects are also play vital roles in heterogeneous catalytic reactions.[19] For example, inorganic graphene analogs (IGA) with high surface atomic percentages have recently been the attention of the world caused by their novel properties[20−24] and huge applications in transistors,[21] energy storage,[22] thermal conductors,[23] and topological insulators.[24] IGAs with a single layer or several layers have been recognized as a new type of nanomaterial due to their unique two-dimensional structural characteristics of atomic thickness.[25−27] These substances show a large proportion of surface atoms and exposed specific faces, which leads to an increase in the density of states at the edge of the valence band, thus promoting the diffusion of the reactants along the 2D conductive channel and the reaction with the dissociated atomic oxygen atoms. These were totally different from those of their bulk counterparts in terms of catalytic oxidation.[27] In addition to this, 2D metal crystals possess abundant coordinatively unsaturated atoms, and the different local atom distributions may lead to completely different electronic structures. Therefore, since the electronic structure is regarded as the most effective axis between the microscopic structure and macroscopic properties and it leads to many exciting applications in energy-related applications, such as energy

storage, energy conversion.[28] In addition, for those who want to understand the real active site and surface reaction mechanism, two-dimensional materials are ideal model catalysts, which can be obtained through theoretical computational chemistry and surface science and technology.[18]

It has been reported that the ultrathin Co_3O_4 sheets showed good activity in oxygen evolution reaction and CO_2 electroreduction.[29] However, it has hardly been applied to any VOC catalytic oxidation reaction. Herein, we prepared a Co_3O_4 sub-nanometer porous sheet (Co_3O_4-SPS) and adopted it to oxidize C_3H_8 considering the large specific surface area, abundant coordinatively unsaturated atoms and surface oxygen vacancies, and superior electron transfer property. As expected, we found that the Co_3O_4-SPS material exhibits extremely high C_3H_8 decomposition activity with C_3H_8 totally converted at just 165 °C and apparent activation energy (E_a) as low as 49.4 kJ mol^{-1}, much better than that of the bulk Co_3O_4 (Co_3O_4-B) catalyst (450 °C and 126.9 kJ mol^{-1}). Experimental and theoretical calculation results reveal that the sub-nanometer porous sheet structure can promote the oxidation reaction by exposing large number of coordinatively unsaturated surface Co atoms as the active sites. At the same time, the larger specific surface area allows the reaction to occur in a larger area, thereby greatly expanding the reaction space.[29] In
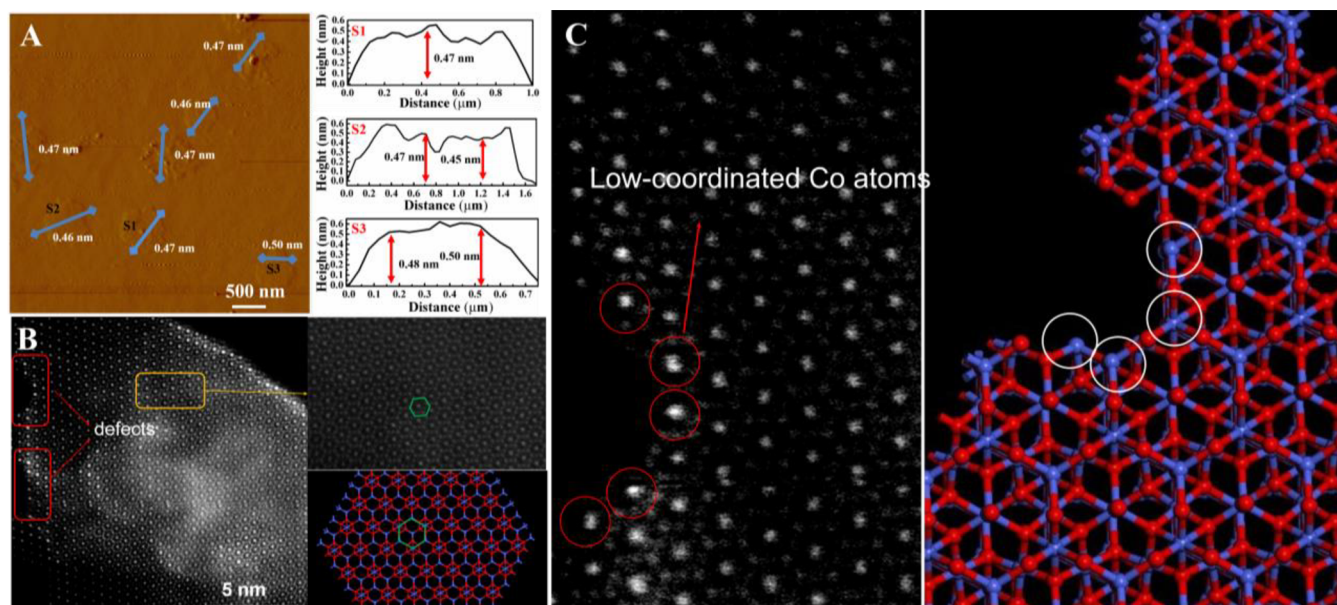
Figure 2. (A) AFM image and (S1−S3) the corresponding height profiles (S1−S3 correspond to the numbers from S1−S3 in Figure 2A); (B) AC-TEM images of Co_3O_4-SPS sample and related theoretical models; (C) local amplification of AC-TEM images and related theoretical models.

addition to this, the density of states (DOS) near the Fermi level in the sub-nanosheet material will be significantly increased by the obvious structural disturbances on the surface, thereby promoting the rapid electron transport along the 2D conductive channel and hence accelerates the reaction kinetics.[18]

2. EXPERIMENTAL SECTION

2.1. Preparation of Catalysts

2.1.1. Synthesis of Co_3O_4 Sub-nanometer Porous Sheets (Co_3O_4-SPS). First, 140 mL of ethylene glycol was dissolved in 28 mL of deionized water, and 700 mg $Co(acac)_3$ was then added and stirred for 60 min. Then the solution was transferred to the Teflon-lined autoclave and heated it at 190 °C for 48 h. After the autoclave is naturally cooled, the precipitate after the reaction was collected by centrifuging the mixture. The collected precipitate was washed with water and ethanol several times and then placed in a vacuum drying oven at 60 °C for 12 h. Then the as-obtained ultrathin CoO sheets were directly heated at 300 °C for 30 min in air and then cooled to the room temperature to obtain the Co_3O_4-SPS.[29]

2.1.2. Synthesis of bulk Co_3O_4(Co_3O_4-B). In a typical procedure,[14] 1 g $Co(NO_3)_2 \cdot 6H_2O$ was heated at 900 °C for 18 h in air and then cooled to the room temperature. The obtained powders were collected for further characterization. The preparation methods of other comparison materials (Co_3O_4 thin sheets, rod-like Co_3O_4, plate-like Co_3O_4, and cube-like Co_3O_4) are listed in Text S1.1 (Supporting Information).

2.2. Catalyst Characterizations

The detailed catalyst characterization techniques including N_2-sorption, X-ray diffraction (XRD), field-emission scanning electron microscopy (FE-SEM), high resolution transmission electron microscopy (HR-TEM), aberration corrected transmission electron microscopy (AC-TEM), atomic force microscopy (AFM), X-ray photoelectron spectroscopy (XPS), Fourier transform infrared (FTIR) absorption spectra, Raman spectra, H_2 temperature-programmed reduction (H_2-TPR), C_3H_8 temperature-programmed surface reaction (C_3H_8-TPSR), *in situ* diffuse reflectance infrared Fourier transform spectra (*in situ* DRIFTS), and X-ray absorption find structure spectra (XAFS) are described in Text S1.2 (Supporting Information).

2.3. DFT Studies

The first-principles calculations were performed by employing the Vienna ab initio simulation package20 using a generalized gradient approximation augmented by a Hubbard U term (GGA+U) with PBE functional, and the detailed methods are described in Text S1.3 (Supporting Information).

2.4. Catalytic Activity

The catalytic activity of prepared catalysts was evaluated in a continuous flow fixed-bed reactor at atmospheric pressure, and the detailed methods are described in Text S1.4 (Supporting Information).

3. RESULTS AND DISCUSSION

3.1. Catalytic Performance

Figure 1A and B shows the catalytic activity of prepared catalysts for the oxidation of C_3H_8. Among the prepared Co_3O_4 catalysts, Co_3O_4-SPS shows the highest catalytic activity with 50% and 90% of C_3H_8 converted at 145 and 160 °C, respectively, which are approximately 175 and 260 °C lower than that of bulk Co_3O_4 (Co_3O_4-B; 320 and 420 °C, respectively). The total conversion and mineralization temperatures (respectively; 165 and 178 °C) of Co_3O_4-SPS for C_3H_8 oxidation are much lower than the reported results in the literature (Table S1). For instance, the total conversion temperature of C_3H_8 over γ-MnO_2,[30] $Co_2Ce_1O_x$[31] and $MnNi_{0.2}O_x$[32] are 325, 275, and 300 °C, respectively. Remarkably, the propane oxidation activity of Co_3O_4-SPS catalyst is even higher than some typical noble metal-loaded catalysts (e.g., the total conversion temperature are respectively of 310, 269, and 275 °C over reported LM-EG,[33] Co_3O_4[34] and 10CoAl-400RO[35] materials).

The C_3H_8 conversion rate can be used to further evaluate the activity of the catalyst, and the corresponding results are shown in Figure 1C. At a reaction temperature of 145 °C, the C_3H_8 conversion rate over Co_3O_4-SPS reaches up to 3.9 × 10^{-10} mol g^{-1}_{cat} s^{-1} (no C_3H_8 conversion can be observed over Co_3O_4-B), which is 2.5 and 10 times higher those that of Co_3O_4-TS (1.5 × 10^{-10} mol g^{-1}_{cat} s^{-1}) and Co_3O_4-R (0.3 ×
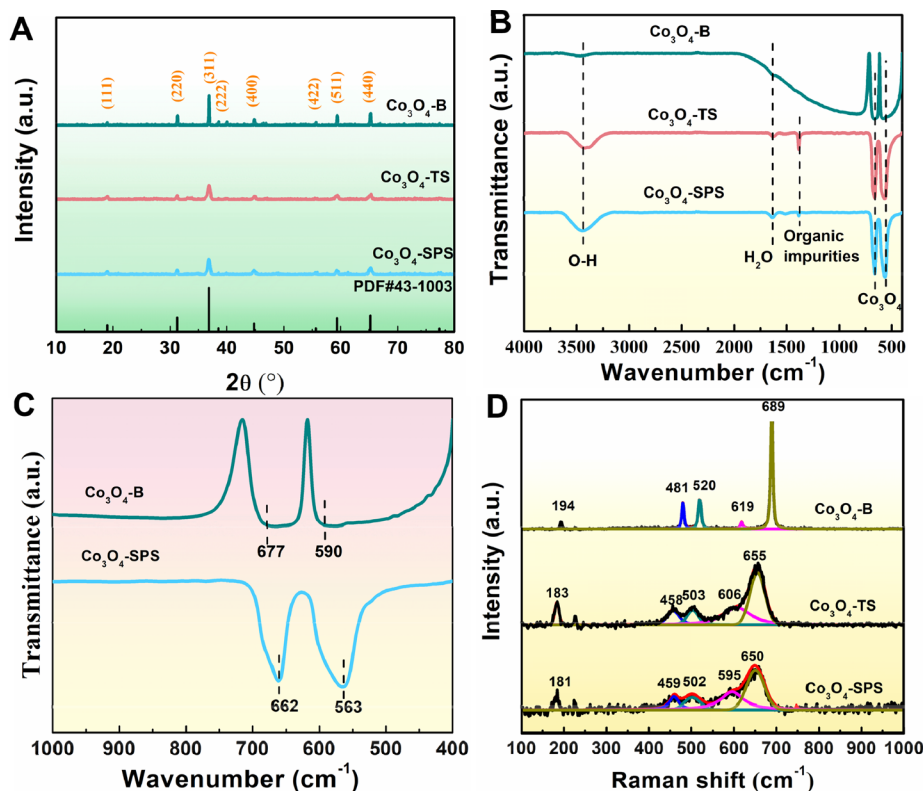
Figure 3. (A) XRD patterns and (B) FT-IR spectra of prepared samples; (C) local FTIR magnification of Co_3O_4-SPS and Co_3O_4-B; (D) Raman spectra of prepared materials.

10^{-10} mol g^{-1}_{cat} s^{-1}), respectively, demonstrating the excellent low-temperature C_3H_8 oxidation activity of the Co_3O_4-SPS catalyst. It is known that the apparent activation energy (E_a) can reflect the difficulty of the reaction. Figure 1D shows that Co_3O_4-SPS has the lowest E_a in C_3H_8 oxidation (49.4 kJ mol^{-1}), which is 1.6 and 2.5 times lower than those of Co_3O_4-TS (82.8 kJ mol^{-1}) and Co_3O_4-B (126.9 kJ mol^{-1}) materials, respectively. The corresponding reaction temperature and C_3H_8 conversion for the calculation of E_a are listed in Table S2.

The stability of the catalysts is another crucial factor judging their catalytic performance. Figure 1E and F shows that almost no deactivation occurs over Co_3O_4-SPS in propane conversion and CO_2 yield during three heating and cooling cycles (temperature range of 40−600 °C) and a 40 h continuous reaction at 190 °C, suggesting the excellent structural and thermal stability, which was further verified by the XRD pattern and TEM images of the used catalysts (Figures S1 and S2). The H_2O resistance results of prepared catalyst are shown in Figure S3, which show that the addition of H_2O (5 and 10 vol %) has little effect on the activity. Also, a complete conversion of propane can be restored shortly when H_2O is no longer added, suggesting that the deactivation of catalyst is reversible. In summary, the experimental results demonstrate that the Co_3O_4-SPS catalyst has excellent reaction stability and water resistance.

3.2. Structural Property

SEM (Figure S4A$_1$) and TEM (Figure S4A$_2$) images indicate that Co_3O_4-SPS possesses a 2D graphene-like morphology and sub-nanostructures. The AFM image and height distribution (Figure 2A) shows that Co_3O_4-SPS material possesses an average height of *ca.* 0.47 nm. The relevant high-precision AFM results are shown in Figure S5. TEM image in Figure

S4A$_2$ clearly demonstrates that there are many holes on the surface of Co_3O_4-SPS with a [111] orientation, confirmed by the corresponding fast Fourier transform image (Figure S4A$_3$, insert) and atomic model (Figure S4A$_4$). The results of AC-TEM (Figure 2B) further prove that the Co_3O_4-SPS catalyst exposes the (111) crystal plane, and its surface porosity leads to a large number of defects. By local amplification of the defect site (Figure 2C), it can be clearly seen that there are abundant low-coordinated Co atoms, and the corresponding theoretical model further proves this result. XRD patterns of prepared materials are shown in Figure 3A, and the (111), (220), (311), (222), (400), (422), (511), and (440) planes attributed to cubic spinel Co_3O_4 (PDF #43-1003) can be observed over all prepared catalysts.

In addition, we explored the synthesis process of the Co_3O_4-SPS catalyst. It can be seen from the experimental results that the ultrathin CoO sheet is the intermediate precursor in the synthesis of Co_3O_4-SPS (Figures S6 and S7A). A previous study concluded that $HOCH_2CH_2OH$ can be partially oxidized to $HOCH_2COOH$ at 190 °C, at which time CoO nucleates,[29] verified by the FTIR spectrum (Figure S7B). Meanwhile, the surface energy of the CoO core can be reduced by adsorbing $HOCH_2COO-$ on its surface. Because of the ionization of the carboxyl group, the existence of $HOCH_2COO-$ can make the CoO core generate a net negative charge.[36] Furthermore, a directional short-range gravitational force will be generated between CoO nuclei due to the hydrogen bonding and van der Waals interaction between $HOCH_2COO-$ species.[36] Then, the CoO nuclei will be driven by the directional short-range attractions and electrostatic interactions to self-assembled into 2D CoO sub-nanometer sheets.[36] After heating at 300 °C in air, CoO will be

Table 1. Textural Properties of Prepared Catalysts

sample	S_{BET} (m^2 g^{-1})[a]	D_v (cm^3 g^{-1})[b]	D_p (nm)[c]	I_{SA-1} ($\times 10^{-12}$ mol m_{cat}^{-2} s^{-1})[d−f]	I_{SA-2} ($\times 10^{-12}$ mol m_{cat}^{-2} s^{-1})[d−f]	I_{SA-3} ($\times 10^{-12}$ mol m_{cat}^{-2} s^{-1})[d−f]
Co_3O_4-SPS	81.3	0.72	15.7	1.47	1.98	4.85
Co_3O_4-TS	50.8	0.38	15.1	0.64	1.68	3.04
Co_3O_4-B	3.7	0.01	9.6			

[a]Specific surface area obtained at P/P_0 = 0.05−0.30. [b]Total pore volume estimated at P/P_0 = 0.99. [c]BJH pore diameter calculated from the desorption branch. [d−f]Specific activity (reaction rate/surface area) of prepared catalysts at 120, 130 and 145 °C, respectively.
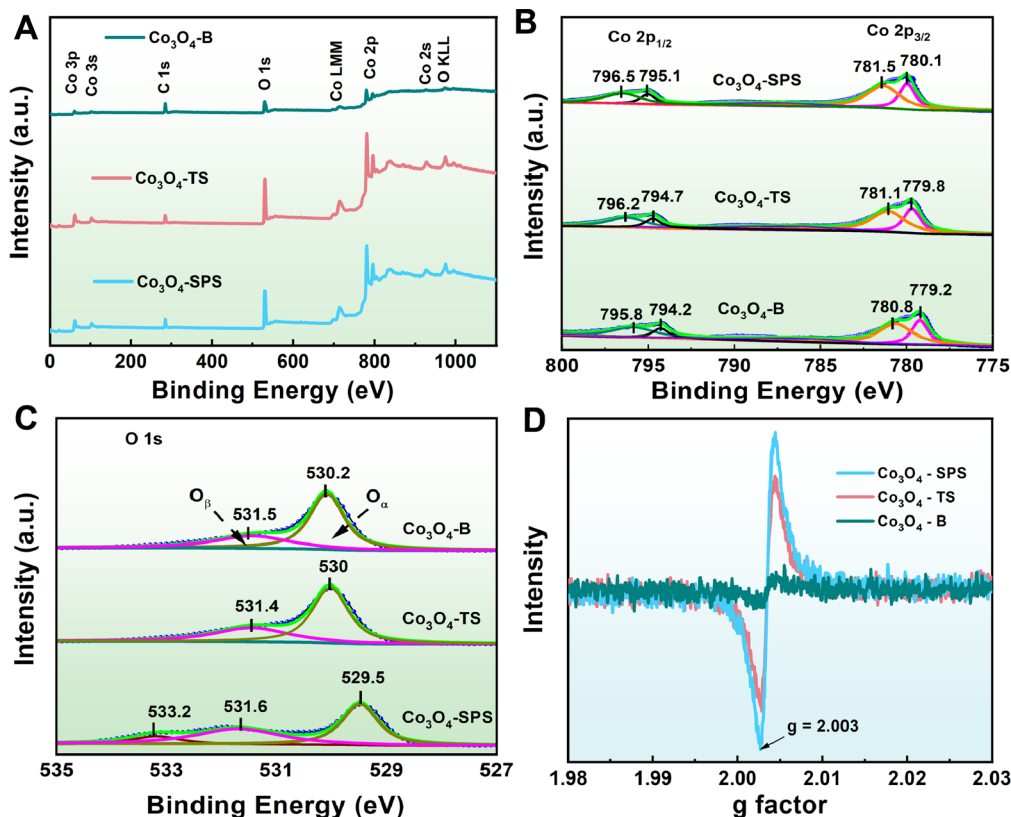

Figure 4. (A) XPS survey spectra; (B) Co 2p and (C) O 1s XPS spectra of prepared catalysts; and (D) ESR spectra of prepared catalysts.

converted to Co_3O_4. At the same time, the combustion or decomposition of $HOCH_2COO-$ will cause many holes on the Co_3O_4 sheets.

In order to understand the mechanism of Co_3O_4 nanocrystals mainly exposing (111) crystal planes, we used theoretical calculation methods to analyze the energy relationship of CoO crystal planes in the $HOCH_2COO-$ system. Previous study shows that the surface energy of CoO follows the order of (100) < (110) < (111)[37] and thus proposed that the (111) plane has the highest activity compared with other crystal planes, indicating that the (111) planes usually decrease rapidly due to the minimization of surface energy during crystal growth. However, in the $HOCH_2COO-$ system, it can be seen that CoO nanocrystals mainly expose the (111) crystal plane. This is mainly because the adsorption capacity of $HOCH_2COO-$ on the (111) plane is stronger than that of the (001) and (110) planes (Figure S8) and the (111) plane can be protected by the adsorption of the surfactant. Then the (111) crystal plane is mainly exposed during the growth of the crystal. Finally, based on the close structural matching, the CoO (111) crystal can be topochemically transformed into (111)-oriented Co_3O_4 (Figure S9).

For comparison, different Co_3O_4 materials, i.e., Co_3O_4 thin sheet (Co_3O_4-TS), Co_3O_4-rod (Co_3O_4-R), Co_3O_4-plate (Co_3O_4-P), Co_3O_4-cube (Co_3O_4-C), and bulk Co_3O_4 (Co_3O_4-B), were also prepared (Figure S10). The specific surface area and porosity of the prepared materials were characterized by low-temperature N_2 sorption, as displayed in Figure S11. It is displayed that all Co_3O_4 samples possess type IV isotherms with clear H3-type hysteresis loops, characteristic of mesoporous materials. The structural properties of the catalysts are displayed in Table 1. It can be seen from the results of specific activity (reaction rate/surface area) that the prepared catalysts follows the order of Co_3O_4-SPS > Co_3O_4-TS ≫ Co_3O_4-B, which indicates that the activity of catalysts is not depend on the surface area and maybe mainly related to their physical and chemical properties.

3.3. Surface Characteristics

FTIR and Raman spectra were employed to investigate the structural and chemical natures of prepared materials. For the FTIR spectra (Figure 3B), the broad band centered at *ca.* 3457 cm^{-1} is attributed to the vibration of O−H bond of water adsorbed on the surface of samples.[38] The peak at 1638 cm^{-1} is assigned to the adsorption of water.[38] The peaks at 1383

pubs.acs.org/jacsau

cm^{-1} can be attributed to the organic impurities left on the surface of the catalyst during the synthesis of the catalyst.[38] The bands in the range 500−800 cm^{-1} are characteristic of the Co−O band vibrations. More specifically, two peaks located at 660−680 and 560−590 cm^{-1} correspond to the stretching vibrations of Co(II)−O and Co(III)−O, respectively.[38] It is noted that the two peaks of Co_3O_4-SPS show a slight red shift toward lower wavenumbers compared to those of Co_3O_4-B (Figure 3C), suggesting a large number of defects on the surface of the nanoparticles, which can weaken the Co−O bond strength.[39]

Five peaks located at 194, 520, 619, 481, and 689 cm^{-1} can be observed over the Co_3O_4-B sample in the Raman spectra, assigned to the $3F_{2g}$, E_g, and A_{1g} modes of Co_3O_4, respectively (Figure 3D).[40] The weak peaks at 194, 520, and 619 cm^{-1} can be regarded as the characteristics of CoO_4, and the peak centered at 689 cm^{-1} can be assigned to the stretching vibration of symmetric CoO_6.[41] In comparison to the Co_3O_4-B sample, the peak positions over Co_3O_4-SPS (respectively; 181, 502, 595, 459, and 650 cm^{-1}) shift to lower wavenumbers by 11−40 cm^{-1} due to the phonon confinement effect evoked by the ultrathin structure.[42] Furthermore, the full width at half maxima (fwhm) values (30−50 cm^{-1}) of Raman spectrum for Co_3O_4-SPS are much higher than those of Co_3O_4-B sample (*ca.* 5−7 cm^{-1}), indicating that the lateral dimensions of these layers are in nanoscale.[42] These data offer reliable evidence for the successful synthesis of Co_3O_4-SPS, in consistentcy with the TEM results (Figure 2). The red shift of Raman peaks also suggests that the original coordinative environment of Co^{2+} and Co^{3+} in lattice of Co_3O_4 has changed, indicating the presence of more crystal defects,[43] in consistent with the results of AC-TEM and FTIR (Figures 2B and 3B). The presence of a larger amount of defects would lead to a higher content of active surface oxygen species on Co_3O_4-SPS, which can promote the catalytic activity for propane oxidation.

The surface composition and chemical status of the prepared samples were investigated by XPS. Figure 4A shows that only Co, C, and O elements can be detected, demonstrating the formation of pure Co_3O_4. Figure 4B shows the Co 2*p* XPS spectra of the prepared catalysts. The main peak at binding energy about 780 eV is characteristic of Co $2p_{3/2}$ with Co^{3+} (779.4 eV) and Co^{2+} (780.8 eV), while the shoulder peak at binding energy of 795 eV is attributed to Co ($2p_{1/2}$).[44] Figure 4C shows the O 1*s* XPS spectra of three samples. The major peak of O 1*s* of Co_3O_4-SPS at about 529.5 eV is assigned to lattice oxygen O_α (O^{2-}), lower than those of Co_3O_4-TS and Co_3O_4-B respectively at at 530 and 530.2 eV. This phenomenon can be attributed to the different combination manners of O^{2-} bonded with Co^{3+} and Co^{2+} on the surface of catalysts (three-coordinated O bonded with three Co^{3+}, O bonded with one Co^{2+} and two Co^{3+}, and two-coordinated O bonded with one Co^{2+} and one Co^{3+}), leading to the binding energy of O^{2-} bonded with Co ions having a considerable difference.[45] From previous studies, it is known that the substantial shift of O_α peak toward to the lower binding energy (*ca.* 529.5 eV), demonstrating that the electrons around the lattice oxygen are easily excited, which can be attributed to the reduction of Co^{3+} to Co^{2+}.[44] This also indicated that the Co−O band of Co_3O_4-SPS are easier to break and then the oxygen vacancies is more likely to occur on Co_3O_4-SPS. Besides, a shoulder peak centered at 531.6 eV can be clearly observed, assigning to the low coordination oxygen species (O_2, O^{2-} and O^-) or oxygen adsorbate residual on oxygen vacancies, in

agreement with the reported results;[45] namely, oxygen vacancies are formed on the surface of Co_3O_4-SPS, Co_3O_4-TS and Co_3O_4-B. The high relative concentration of oxygen vacancies on the surface of catalyst can be correlated with the high activity in the oxidation reaction.[45]

It is shown in Table 2 that the ratios of O_β/O_α are approximately 0.89, 0.54, and 0.49 for Co_3O_4-SPS, Co_3O_4-TS,

Table 2. XPS Results of the Prepared Catalysts

	binding energy (eV)					
sample	Co^{3+} $2p_{3/2}$	Co^{2+} $2p_{3/2}$	O_α	O_β	$Co^{2+}/$ Co^{3+}	$O_\beta/$ O_α
Co_3O_4-B	780.1	781.5	530.2	531.5	1.72	0.44
Co_3O_4-TS	779.8	781.1	530.0	531.4	1.76	0.54
Co_3O_4-SPS	779.2	780.8	529.5	531.6	1.82	0.89

and Co_3O_4-B, respectively, suggesting that there are largest amount of oxygen vacancy species existed over the Co_3O_4-SPS. Accordingly, the Co^{2+}/Co^{3+} surface ratio of Co_3O_4-SPS is determined to be 1.82, which is higher than that of Co_3O_4-B (1.72), indicating that there are more surface oxygen vacancies which are balanced by the conversion of Co^{3+} to Co^{2+} on Co_3O_4-SPS.[46] ESR was carried out to further explain the oxygen vacancy concentration of prepared materials (Figure 4D), and the results show that the Co_3O_4-SPS catalyst has the highest oxygen vacancy concentration.

XAFS and DFT were further employed to investigate their structural and chemical nature. As shown by Co K-edge EXAFS (Figure 5A), the postedge oscillation amplitude for the Co_3O_4-SPS exhibits obvious differences in comparison with the Co_3O_4-B ascribed to the structural difference between Co_3O_4-SPS and Co_3O_4-B.[47] Co_3O_4-SPS has a lower Co−O coordination number of Co atoms on the surface compared to that of Co_3O_4-B. Moreover, the results of the corresponding Co K-edge $k^3\chi(k)$ oscillation curve and Fourier transformed $k^3\chi(k)$ functions (Figure 5B,C) also confirm a lower Co−O coordination number of Co atoms on the Co_3O_4-SPS surface and quantitatively reveal their distinct local atomic arrangement. Three peaks located at *ca.* 1.51, 2.51, and 3.04 Å are considered to be characteristics of Co_3O_4. In detail, the peaks at 2.51 and 3.04 Å are attributed to the Co−Co bond and the one at 1.51 Å is related to the Co−O coordination in the first coordination shell.[47] Obviously, the intensity of Co−O coordination peaks over Co_3O_4-SPS decreases significantly compared to those of the Co_3O_4-TS and Co_3O_4-B due to the surface structural disorder of Co_3O_4-SPS (Figure 2A_2).[48]

In order to obtain the structural parameters around the Co atoms on the surface of the Co_3O_4-SPS sample, we performed a least-squares curve fitting (Figure S12), and the fitting results are documented in Table 3. It is found that, due to the existence of abundant lattice defects (Figure 2C), a large number of low coordination atoms are generated, which reduce the local coordination number.[48] XPS results prove that Co_3O_4-SPS has abundant oxygen deficiencies (Figure 4C). For the Co_3O_4-SPS sample, the reduction of Co−O, Co−Co_1, and Co−Co_2 coordination number and increase in disorder degrees suggested its surface has a large number of dangling bonds and obvious distortion,[49] which in turn helps to create excellent structural stability.[44] Undoubtedly, the surface distortion of Co_3O_4 layer significantly influences its electronic properties.[49] In addition, as shown in Figure 5D, the results of DFT calculations indicated that the state density of the
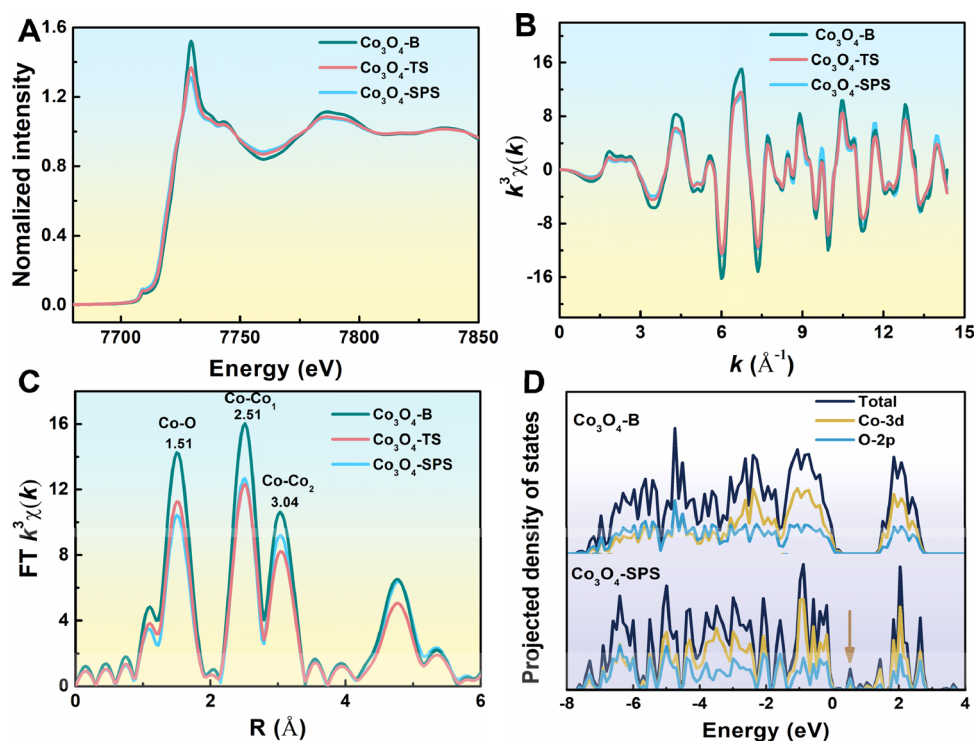
Figure 5. (A) Co K-edge XANES, (B) Co K-edge EXAFS, (C) Fourier transform of the EXAFS data in (B), and (D) calculated DOS of prepared catalysts.

Table 3. EXAFS Fitting Parameters at the Co K-Edge of Prepared Catalysts

sample	shell	N^a	R (Å)^b	σ^2 (Å^2· 10^{-3})^c	ΔE_0 (eV)^d
Co_3O_4-B	Co—O	5.6 ± 0.2	1.92 ± 0.03	3.2 ± 0.2	5.1
	Co—Co$_1$	4.0 ± 0.2	2.85 ± 0.03	3.1 ± 0.2	3.9
	Co—Co$_2$	10.8 ± 0.2	3.35 ± 0.03	8.0 ± 0.2	1.5
Co_3O_4-TS	Co—O	4.3 ± 0.2	1.92 ± 0.03	2.8 ± 0.2	4.8
	Co—Co$_1$	3.4 ± 0.2	2.86 ± 0.03	3.5 ± 0.2	3.6
	Co—Co$_2$	7.2 ± 0.2	3.35 ± 0.03	7.0 ± 0.2	1.6
Co_3O_4-SPS	Co—O	3.7 ± 0.2	1.95 ± 0.03	2.5 ± 0.2	4.7
	Co—Co$_1$	2.7 ± 0.2	2.85 ± 0.03	2.1 ± 0.2	3.2
	Co—Co$_2$	7.9 ± 0.2	3.35 ± 0.03	7.0 ± 0.2	0.7

^{a}Coordination numbers. ^{b}Bond distance. ^{c}Debye—Waller factors. ^{d}Inner potential correction.

ultrathin Co_3O_4 layer at the edge of the conduction band is significantly higher than the bulk phase. Moreover, the results of partial charge density (Figure S13) also demonstrate that the charge density in the ultrathin Co_3O_4 layer increases noticeably compared with Co_3O_4-B.

The high density of states at the edge of the valence band and conduction band (Figure S14) means that the surface polarization of the catalyst is strong, and the catalysts need to be depolarized to a stable state through the flow of free charges in the surface layer, so that the surface of the catalyst has strong metal properties, which is conducive to the transfer of electrons.[4,32] Through the charge density difference diagram and better charge analysis (Figure S15), it can be concluded that this surface electronic state is beneficial to the charge transfer between the catalyst surface and the reactant molecules. The surface electron density of more low-coordinated Co atoms on the surface of Co_3O_4-SPS which also exhibits metallic properties can also causes an imbalance in

the charge distribution at the interface, generating a built-in electric field around the low-coordinated Co atoms and promoting the transfer of electrons.[50] As shown in Figure S16, Co_3O_4-SPS has a larger CV curve integral area and a stronger current density than Co_3O_4-B, indicating that Co_3O_4-SPS possesses a stronger electron conduction capability. The accelerated electron transport at the interface can facilitate oxygen activation and the redox cycle of Co^{3+}/Co^{2+} during the catalytic reaction, thereby promoting catalytic oxidation of propane.[51,52] After fitting the experimental data, the bond distances of Co—O, Co—Co$_1$, and Co—Co$_2$ of different catalysts were obtained and are listed in Table 3. It can be observed that the Co—O band of Co_3O_4-SPS is slightly elongated compared with the Co_3O_4-B, indicating there are a lot of lattice distortions on the surface of Co3O4-SPS, which may be caused by many defects on the surface of Co_3O_4-SPS (Figure 2C). The slight elongation of the Co—O band in Co_3O_4-SPS also indicates that the Co—O bands are easier to break and form oxygen vacancies compared with other catalysts.

3.4. Reducibility

Reducibility of the prepared catalysts was tested by H_2-TPR, as shown in Figure 6. The reduction process of Co_3O_4-B can be reasonably divided into two stages of Co^{3+} to Co^{2+} and Co^{2+} to Co (Figure 6A).[45] Co_3O_4-SPS possesses the best low-temperature reducibility with the first reduction peak centered at 292 °C, much lower than that of the other catalysts (313–427 °C). It is demonstrated that the Co—O band in Co_3O_4-SPS is easier to break and therefore releases lattice oxygen to create oxygen deficiency, accelerating the reduction of Co^{3+} to Co^{2+}.[45] To compare the low temperature reducibility of synthesized catalysts more efficiently, we calculated the initial H_2 consumption rate of the first reduction zone of each sample before the phase transition (where the initial H_2 consumption
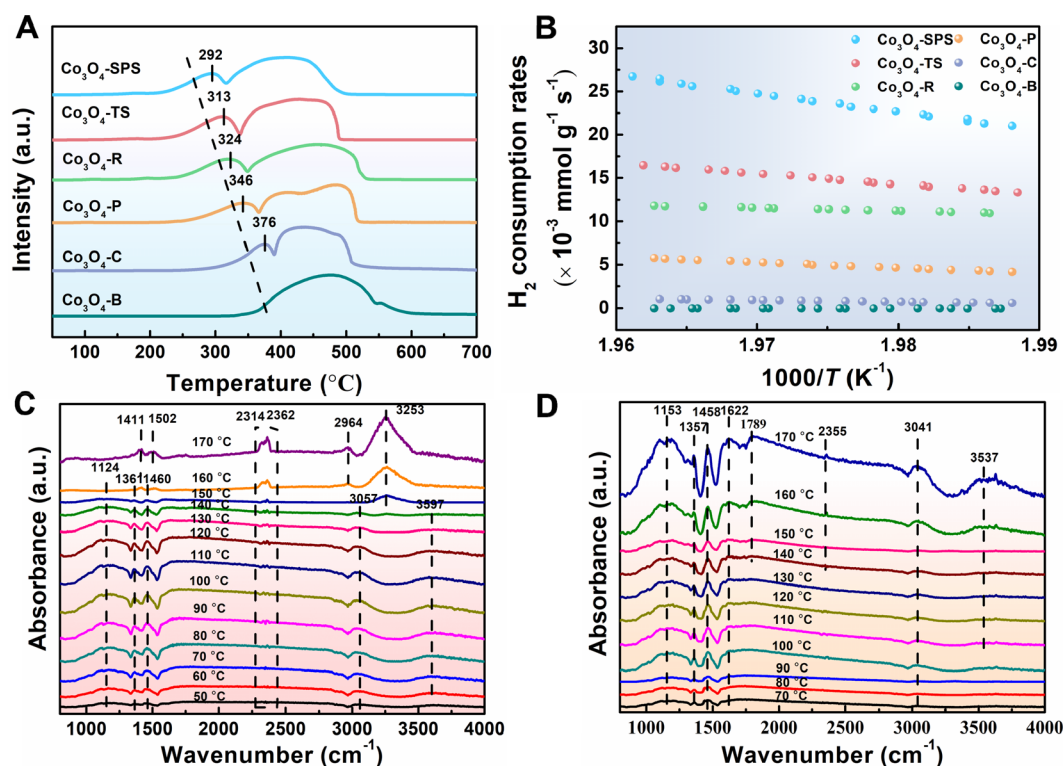
Figure 6. (A) H_2-TPR and (B) initial H_2 consumption rates of prepared catalysts; *in situ* DRIFTS of (C) Co_3O_4-SPS and (D) Co_3O_4-B for C_3H_8 oxidation.

of the first reduction band of catalyst is less than 25%),[53,54] as shown in Figure 6B. It can be noted that the initial H_2 consumption rate of Co_3O_4-SPS is much higher than the other catalysts, suggesting the superior low-temperature reducibility.

3.5. Reaction Mechanism

The reaction route and intermediate distribution were determined by C_3H_8-TPSR and *in situ* DRIFTS. C_3H_8-TPSR was performed to explore the reduction behaviors of prepared samples under a flowing of C_3H_8, as presented in Figure S17. For the Co_3O_4-SPS sample, the first C_3H_8 consumption peak is assigned to the reaction between surface adsorbed oxygen and C_3H_8. The presence of a strong peak with m/z of 44 (CO_2) and a negative peak with m/z of 29 (C_3H_8) indicates that the total oxidation of C_3H_8 occurred (Figure S15A).[55] Previous work claimed that the oxygen adsorbed on catalyst surface defect sites is mainly the reactive oxygen species.[55,56] Active oxygen mainly exists in the form of adatoms, such as O_2^-, and O^-, which are highly electrophilic. Active oxygen can extract hydrogen from alkanes to form alkenes, then they will undergo a continuous oxidation reactions to CO_2.[57,58] The strong positive peaks (m/z = 44 and 28) and negative peaks (m/z = 29) appeared at about 320 °C, suggesting that at this temperature, C_3H_8 reacts with the lattice oxygen in Co_3O_4 to generate CO_2. The main active oxygen species at this time is the lattice oxygen (O^{2-}), which is nucleophilic oxide ions and has a high oxidative dehydrogenation rate during the deep oxidation process.[58] Similar results can also be observed in C_3H_8-TPSR spectra of Co_3O_4-B sample (Figure S17B), but all related peaks shift to much higher temperatures. It is indicated that both C_3H_8 and surface adsorbed oxygen are more easily activated on the Co_3O_4-SPS sample.

In situ DRIFT spectra of C_3H_8 oxidation over Co_3O_4-SPS and Co_3O_4-B materials were performed to clarify the C_3H_8 adsorption and decomposition processes. As shown in Figure 6C and D, the bands at 3057 and 3041 cm^{-1} are related to the C–H stretching vibrations of adsorbed C_3H_8.[59] The bands at 1361 and 1460 cm^{-1} can be attributed to the $\delta(CH)$ species,[60] and the bands at 1124 and 1153 cm^{-1} can be assigned to $\upsilon C–C$.[61] The bands at 2313 and 2362 cm^{-1} are assigned to gaseous CO_2, suggesting the oxidation of C_3H_8 happened.[59] The band at 3597 and 3537 cm^{-1} can be attributed to the –OH bond vibration adsorbed on the catalyst surface.[58] It is shown that the formation of CO_2 started at 70 and 170 °C for Co_3O_4-SPS and Co_3O_4-B, respectively, indicating the excellent low-temperature activity of Co_3O_4-SPS, in good agreement with the light-off curves (Figure 1A). For Co_3O_4-SPS, the bands at 1124, 1361, 1460, and 3057 cm^{-1} first increase and then decrease, and four new peaks (2964, 3253, 1411, and 1502 cm^{-1}) appeared when the temperature reaches 160 °C. The peak at 2964 cm^{-1} can be attributed to the C–H stretching vibrations of formate species.[62] The peaks at 1502 (υ_{as} COO^-) and 1411 cm^{-1} (υ_{sym} COO^-) can be assigned to the carboxylate which may come from acetate and formate species,[61,63] which are important precursors for CO_2. This means that, in the whole reaction process, with the increase of the reaction temperature from 50 to 120 °C, the consumption of propane increases. With the further increase of the temperature from 120 to 170 °C, the $\delta(CH)$ species is oxidized to COO^- (comes from acetate and formate species) by reactive oxygen species; COO^- species at around 1411 and 1502 cm^{-1} increase, which leads to the decrease of the other positive peaks of propane. The band at 3253 cm^{-1} can be attributed to the OH^- species of H_2O produced after the oxidation of C_3H_8 on catalyst surface.[64]
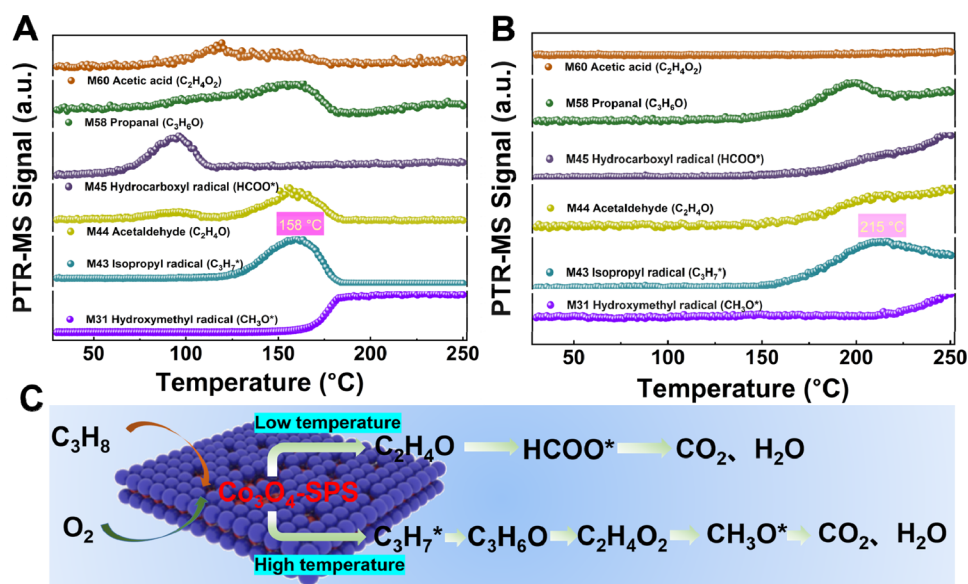
Figure 7. (A, B) PTR-QMS for C_3H_8 oxidation at 30−250 °C over Co_3O_4-SPS and Co_3O_4-B; (C) degradation pathway of propane over the Co_3O_4-SPS catalyst.
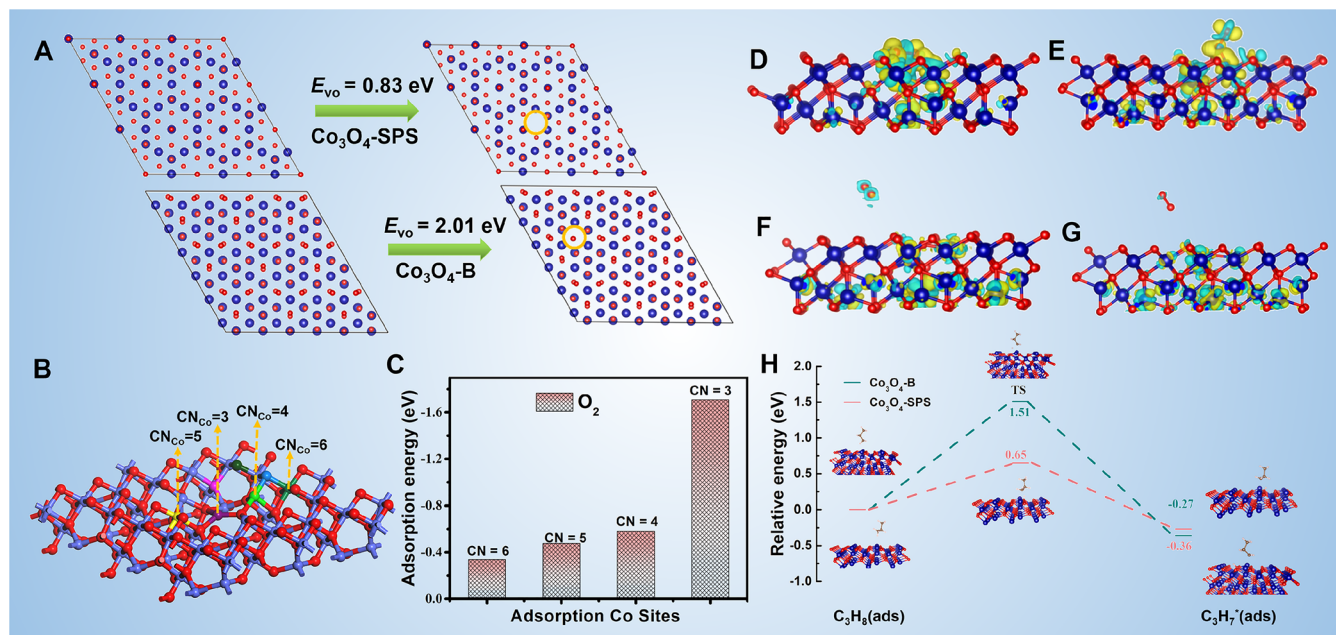

Figure 8. (A) Formation energy of oxygen vacancy over Co_3O4-SPS and Co_3O4-B; (B) coordination numbers of surface and pore surrounding Co atoms; (C) adsorption energy of O_2 molecules on Co sites with different coordination numbers (CN); corresponding charge-density difference diagram of oxygen adsorption over various Co sites: (D) CN = 3, (E) CN = 4, (F) CN = 5, and (G) CN = 6 (red atoms are O atoms, blue atoms are Co atoms); (H) potential energy profiles for the adsorption and dissociation of propane ($C_3H_8 \rightarrow C_3H_7 + H$) on Co_3O_4-SPS and Co_3O_4-B, respectively.

For bulk Co_3O_4, however, all peaks increase gradually with the increasing of temperature, indicating that the C_3H_8 molecule is only adsorbed but not decomposed in this temperature range. Based on the above results, it is proposed that the adsorbed C_3H_8 can be deeply oxidized to CO_2 by surface adsorbed oxygen at low temperature, while in the high temperature range of >150 °C, the adsorbed C_3H_8 is activated and oxidized to carbonate intermediate products over active oxygen, and then are further converted into CO_2 and H_2O. Combining the results of C_3H_8-TPSR, it is indicated that the activated propane molecule is oxidized by dissociatively

chemisorbed oxygen to form carbon dioxide and water when the temperature reaches 150 °C. Finally, as can be seen from the activity diagram, the activity showes a sharp increase at 150 °C. Combined with previous studies,[55] it can be concluded that the breaking of the C−H bonds at this temperature is the rate-determining step of the entire active reaction.

In order to further prove the above conclusions, we carried out PTR-QMS experiments to detect the intermediate species produced during the catalytic degradation process (Figure 7). It can be seen from Figure 7A and B that, in the low temperature section (50−150 °C), the catalytic degradation of

propane on Co_3O_4-SPS produces intermediate products such as HCOO* and C_2H_4O, while no intermediate products are produced on the Co_3O_4-B sample. This phenomenon is consistent with the *in situ* DRIFTS results. Combined with the results of C_3H_8-TPSR, it is further proved that, compared with Co_3O_4-B catalyst, the Co_3O_4-SPS catalyst more easily activates surface adsorbed oxygen at low temperature, thus further activating propane. From the formation temperature of C_3H_7* species, it can be seen that the Co_3O_4-SPS catalyst more easily activates the C−H bonds of propane, which is consistent with the results of *in situ* DRIFTS. When the C−H bonds of propane are activated, C_3H_6O, $C_2H_4O_2$, and CH_3O* intermediate products appear during the degradation of propane on both catalysts. From the above conclusions, it can be inferred that the degradation path of propane on Co_3O_4-SPS catalyst is as follows (Figure 7C): at a low temperature range, propane is activated by active oxygen on the surface of the catalyst to form HCOO* and C_2H_4O, which is further mineralized to CO_2 and H_2O; at a high temperature range (≥ 150 °C), C−H bonds are activated to form intermediate products such as C_3H_6O, $C_2H_4O_2$, and CH_3O*, and then deeply oxidized to CO_2 and H_2O. Therefore, the activation of both surface adsorbed oxygen and C_3H_8 (C−H cracking) plays an important role in C_3H_8 low-temperature oxidation.

3.6. DFT Calculations

Oxygen vacancies are suggested to play an important role in propane decomposition.[4] In the present work, the formation energy of a single oxygen defect over Co_3O_4-SPS exposed facets was studied by DFT calculations, as shown in Figure 8A. Results demonstrate that the formation energy of oxygen vacancy on surface of Co_3O_4-SPS (E_{vo} (110) = 0.83 eV) is obviously lower than that of Co_3O_4-B facet (E_{vo}(111) = 2.01 eV), indicating that the oxygen vacancies more easily form on the surface of Co_3O_4-SPS. These oxygen vacancies will activate more adsorbed oxygen and as a consequence accelerate the activation process of propane molecules over Co_3O_4-SPS, consistent with the results of H_2-TPR (Figure 6) and C_3H_8-TPSR (Figure S17).

As mentioned above, the activation of surface adsorbed oxygen and efficient C−H cracking are critical steps in the catalytic oxidation of C_3H_8. The chemical adsorption of O_2 and disassociation of C−H bond were studied by DFT. The EXAFS fitting results reveal that the presence of structural pores decreases the coordination number of Co atoms from 6 to 4 or even 3 in Co_3O_4-SPS (Figure 8B). It is well-documented that the adsorption capacity of oxygen is an important parameter for oxygen activation in VOC oxidation reaction.[4] Figure 8C displays the oxygen adsorption on different cocoordinated Co atoms. It is found that as the Co coordination number (CN) decreases from 6 to 3, their adsorption energy for oxygen gradually increases. The adsorption energy of the 3-coordinated Co atom is −1.71 eV, which is significantly greater than that of the 4-coordinated Co atom (−0.58 eV), 5-coordinated Co atom (−0.47 eV) and 6-coordinated Co atom (−0.33 eV). It is indicated that the low-coordination surface Co atoms can be used as catalytically active sites to maximize the activation of adsorbed O_2 so that they can effectively participate in the VOC oxidation reaction.[4]

In order to gain further insights into the effect of different cocoordinated Co atoms toward activating adsorbed oxygen, the corresponding charge-density difference diagram of oxygen adsorption on different coordinated Co atoms was calculated, as shown in Figure 8D−G. Results show that oxygen has a strong interaction with 3-coordinated Co atoms compared with the other coordinated Co atoms. As shown in Figure 8D, a strong electron coupling effect can be observed at the interface between 3-coordinated Co atoms and oxygen molecule, which could activate the adsorbed oxygen molecules easily.[29] This is also confirmed by the change of the O−O bond length displayed in Figure S18. The three-coordinated Co atom is firmly bonded with O_2, and the O−O bond distance is 1.436 Å. It is longer than that on the 4-coordinated Co atom (1.268 Å), 5-coordinated Co atom (1.230 Å), and 6-coordinated Co atom (1.226 Å), indicating that the low-coordination Co atoms can more easily destroy and activate the adsorbed O_2.

On the other hand, C−H cracking is the critical step in activating the C_3H_8 molecule. As shown in Figure 8H. The DFT results show that the C−H bond is easier to break on Co_3O_4-SPS (E_{dis} (dissociation energies of C−H) = 0.65 eV) than that of Co_3O_4-B (E_{dis} = 1.51 eV). The corresponding configurations of C_3H_8(ads), TS, and C_3H_7(ads) are shown in Figure S19. It is generally believed that the activation of hydrocarbon molecules on oxide catalysts occurs at a center containing MO acid−base pairs, and the oxide ion (O) functions as the abstract center of hydrogen atoms, while the cationic center (M) promotes electron transfer.[65] Theoretical calculation reveals that Co_3O_4-SPS has a higher surface electron density than that of Co_3O_4-B, suggesting the higher surface basicity,[65] which favors the activation of hydrocarbons.[66] The higher DOS at the conduction band edges can facilitate electron transport[29] and increase the interaction of electron pairs between σ and σ* C−H orbitals with transition metal cations and can break C−H bonds more easily.[29]

4. CONCLUSIONS

In brief, the Co_3O_4 sub-nanometer porous sheet (Co_3O_4-SPS) was fabricated and demonstrated as a robust catalyst in C_3H_8 decomposition with the total oxidation temperature and apparent activation energy being, respectively, as low as 165 °C and 49.4 kJ mol^{-1}. XAFS and DFT results reveal that the abundant low-coordinate surface Co atoms favor O_2 adsorption and dissociation into highly reactive oxygen atoms. Moreover, the surface disorder of Co_3O_4-SPS leads to the enhancement of its surface metal properties, which is conducive to the transmission of electrons on its surface, resulting in more electron transfer between the catalyst surface and the reactant molecules. Based on these, the C−H bonds in C_3H_8 can be cracked more easily over Co_3O_4-SPS, which is crucial for subsequent reactions. In addition, Co_3O_4-SPS also has excellent thermal stability and water resistance. The present work provides atomic-level insights into the low-temperature decomposition of C_3H_8 over Co_3O_4-SPS and further sheds new tactics for developing efficient catalysts for VOC purification and other thermocatalytic oxidation reactions.

■ ASSOCIATED CONTENT

ⓢ Supporting Information

The Supporting Information is available free of charge at https://pubs.acs.org/doi/10.1021/jacsau.3c00471.

Catalyst preparation, characterizations, and catalytic activity of prepared materials; XRD and TEM results of fresh and used Co_3O_4-SPS sample; XRD, TEM, FTIR and DFT results of ultrathin CoO sheets; nitrogen adsorption−desorption isotherms and pore size of prepared materials; Co K edge curve fitting results of samples; Partial charge density diagram of Co_3O_4-SPS and Co_3O_4-B; and the adsorption energy of O_2 on different coordinated Co atoms on Co_3O_4-SPS catalyst (PDF)

AUTHOR INFORMATION

Corresponding Author

Chi He − *State Key Laboratory of Multiphase Flow in Power Engineering, Xi'an Jiaotong University, Xi'an 710049 Shaanxi, P.R. China; National Engineering Laboratory for VOCs Pollution Control Material & Technology, University of Chinese Academy of Sciences, Beijing 101408, P.R. China;* orcid.org/0000-0001-6403-1277; Phone: +86 29 82663857; Email: chi_he@xjtu.edu.cn

Authors

Yanfei Jian − *State Key Laboratory of Multiphase Flow in Power Engineering, Xi'an Jiaotong University, Xi'an 710049 Shaanxi, P.R. China;* orcid.org/0009-0009-1039-2662

Zeyu Jiang − *State Key Laboratory of Multiphase Flow in Power Engineering, Xi'an Jiaotong University, Xi'an 710049 Shaanxi, P.R. China;* orcid.org/0000-0002-9997-2357

Mingjiao Tian − *State Key Laboratory of Multiphase Flow in Power Engineering, Xi'an Jiaotong University, Xi'an 710049 Shaanxi, P.R. China*

Mudi Ma − *State Key Laboratory of Multiphase Flow in Power Engineering, Xi'an Jiaotong University, Xi'an 710049 Shaanxi, P.R. China*

Lianghui Xia − *State Key Laboratory of Multiphase Flow in Power Engineering, Xi'an Jiaotong University, Xi'an 710049 Shaanxi, P.R. China*

Shouning Chai − *State Key Laboratory of Multiphase Flow in Power Engineering, Xi'an Jiaotong University, Xi'an 710049 Shaanxi, P.R. China*

Jingjing Wang − *State Key Laboratory of Multiphase Flow in Power Engineering, Xi'an Jiaotong University, Xi'an 710049 Shaanxi, P.R. China*

Reem Albilali − *Department of Chemistry, College of Science, Imam Abdulrahman Bin Faisal University, Dammam 31441, Saudi Arabia*

Complete contact information is available at:
https://pubs.acs.org/10.1021/jacsau.3c00471

Notes

The authors declare no competing financial interest.

REFERENCES

(1) Liotta, L. F. Catalytic oxidation of volatile organic compounds on supported noble metals. *Appl. Catal., B* **2010**, *100*, 403−412.

(2) He, C.; Cheng, J.; Zhang, X.; Douthwaite, M.; Pattisson, S.; Hao, Z. Recent Advances in the Catalytic Oxidation of Volatile Organic Compounds: A Review Based on Pollutant Sorts and Sources. *Chem. Rev.* **2019**, *119*, 4471−4568.

(3) Jiang, Z.; Feng, X.; Deng, J.; He, C.; Douthwaite, M.; Yu, Y.; Liu, J.; Hao, Z.; Zhao, Z. Atomic-Scale Insights into the Low-Temperature Oxidation of Methanol over a Single-Atom Pt_1-Co_3O_4 Catalyst. *Adv. Funct. Mater.* **2019**, *29*, 1902041.

(4) Jian, Y.; Yu, T.; Jiang, Z.; Yu, Y.; Douthwaite, M.; Liu, J.; Albilali, R.; He, C. In-Depth Understanding of the Morphology Effect of alpha-Fe_2O_3 on Catalytic Ethane Destruction. *ACS Appl. Mater. Interfaces* **2019**, *11*, 11369−11383.

(5) Feng, X.; Chen, C.; He, C.; Chai, S.; Yu, Y.; Cheng, J. Non-thermal plasma coupled with MOF-74 derived Mn-Co-Ni-O porous composite oxide for toluene efficient degradation. *J. Hazard Mater.* **2020**, *383*, 121143.

(6) Feng, X.; Tian, M.; He, C.; Li, L.; Shi, J. W.; Yu, Y.; Cheng, J. Yolk-shell-like mesoporous $CoCrO_x$ with superior activity and chlorine resistance in dichloromethane destruction. *Appl. Catal., B* **2020**, *264*, 118493.

(7) Hu, Z.; Qiu, S.; You, Y.; Guo, Y.; Guo, Y.; Wang, L.; Zhan, W.; Lu, G. Hydrothermal synthesis of $NiCeO_x$ nanosheets and its application to the total oxidation of propane. *Appl. Catal., B* **2018**, *225*, 110−120.

(8) Park, J. E.; Kim, K. B.; Kim, Y. A.; Song, K. S.; Park, E. D. Effect of Pt Particle Size on Propane Combustion Over Pt/ZSM-5. *Catal. Lett.* **2013**, *143*, 1132−1138.

(9) Taylor, M. N.; Zhou, W.; Garcia, T.; Solsona, B.; Carley, A. F.; Kiely, C. J.; Taylor, S. H. Synergy between tungsten and palladium supported on titania for the catalytic total oxidation of propane. *J. Catal.* **2012**, *285*, 103−114.

(10) Tang, W.; Xiao, W.; Wang, S.; Ren, Z.; Ding, J.; Gao, P. X. Boosting catalytic propane oxidation over PGM-free Co_3O_4 nano-crystal aggregates through chemical leaching: A comparative study with Pt and Pd based catalysts. *Appl. Catal., B* **2018**, *226*, 585−595.

(11) Zhu, Q.; Jiang, Z.; Ma, M.; He, C.; Yu, Y.; Liu, X.; Albilali, R. Revealing the unexpected promotion effect of diverse potassium precursors on α-MnO_2 for the catalytic destruction of toluene. *Catal. Sci. Technol.* **2020**, *10*, 2100−2110.

(12) Haneda, M.; Kintaichi, Y.; Bion, N.; Hamada, H. Alkali metal-doped cobalt oxide catalysts for NO decomposition. *Appl. Catal., B* **2003**, *46*, 473−482.

(13) Xie, X.; Li, Y.; Liu, Z. Q.; Haruta, M.; Shen, W. Low-temperature oxidation of CO catalysed by Co_3O_4 nanorods. *Nature* **2009**, *458*, 746−9.

(14) Xie, X.; Shen, W. Morphology control of cobalt oxide nanocrystals for promoting their catalytic performance. *Nanoscale* **2009**, *1*, 50−60.

(15) Wang, X.; Tian, W.; Zhai, T.; Zhi, C.; Bando, Y.; Golberg, D. Cobalt(ii,iii) oxide hollow structures: fabrication, properties and applications. *J. Mater. Chem.* **2012**, *22*, 23310−23326.

(16) Solsona, B.; Davies, T. E.; Garcia, T.; Vázquez, I.; Dejoz, A.; Taylor, S. H. Total oxidation of propane using nanocrystalline cobalt oxide and supported cobalt oxide catalysts. *Appl. Catal., B* **2008**, *84*, 176−184.

(17) Hu, Z.; Wang, Z.; Guo, Y.; Wang, L.; Guo, Y.; Zhang, J.; Zhan, W. Total Oxidation of Propane over a Ru/CeO_2 Catalyst at Low Temperature. *Environ. Sci. Technol.* **2018**, *52*, 9531−9541.

(18) Wang, Y.; Mao, J.; Meng, X.; Yu, L.; Deng, D.; Bao, X. Catalysis with Two-Dimensional Materials Confining Single Atoms: Concept, Design, and Applications. *Chem. Rev.* **2019**, *119*, 1806−1854.

(19) Sun, Y.; Lei, F.; Gao, S.; Pan, B.; Zhou, J.; Xie, Y. Atomically thin tin dioxide sheets for efficient catalytic oxidation of carbon monoxide. *Angew. Chem., Int. Ed. Engl.* **2013**, *52*, 10569−72.

(20) Sun, Y.; Sun, Z.; Gao, S.; Cheng, H.; Liu, Q.; Piao, J.; Yao, T.; Wu, C.; Hu, S.; Wei, S.; Xie, Y. Fabrication of flexible and freestanding zinc chalcogenide single layers. *Nat. Commun.* **2012**, *3*, 1057.

(21) Radisavljevic, B.; Radenovic, A.; Brivio, J.; Giacometti, V.; Kis, A. Single-layer MoS$_2$ transistors. *Nat. Nanotechnol* **2011**, *6*, 147−50.

(22) Zhu, Y. W.; Murali, S.; Stoller, M. D.; Ganesh, K. J.; Cai, W. W.; Ferreira, P. J.; Pirkle, A.; Wallace, R. M.; Cychosz, K. A.; Thommes, M.; Su, D.; Stach, E. A.; Ruoff, R. S. Carbon-Based Supercapacitors Produced by Activation of Graphene. *Science* **2011**, *332*, 1537−1541.

(23) Zhi, C.; Bando, Y.; Tang, C.; Kuwahara, H.; Golberg, D. Large-Scale Fabrication of Boron Nitride Nanosheets and Their Utilization in Polymeric Composites with Improved Thermal and Mechanical Properties. *Adv. Mater.* **2009**, *21*, 2889−2893.

(24) Wang, G.; Zhu, X. G.; Sun, Y. Y.; Li, Y. Y.; Zhang, T.; Wen, J.; Chen, X.; He, K.; Wang, L. L.; Ma, X. C.; Jia, J. F.; Zhang, S. B.; Xue, Q. K. Topological insulator thin films of Bi$_2$Te$_3$ with controlled electronic structure. *Adv. Mater.* **2011**, *23*, 2929−32.

(25) Zhu, J. B.; Bai, L. F.; Sun, Y. F.; Zhang, X. D.; Li, Q. Y.; Cao, B. X.; Yan, W. S.; Xie, Y. Topochemical transformation route to atomically thick Co$_3$O$_4$ nanosheets realizing enhanced lithium storage performance. *Nanoscale* **2013**, *5*, 5241−5246.

(26) Rui, X.; Lu, Z.; Yin, Z.; Sim, D. H.; Xiao, N.; Lim, T. M.; Hng, H. H.; Zhang, H.; Yan, Q. Oriented molecular attachments through sol-gel chemistry for synthesis of ultrathin hydrated vanadium pentoxide nanosheets and their applications. *Small* **2013**, *9*, 716−21.

(27) Feng, J.; Sun, X.; Wu, C.; Peng, L.; Lin, C.; Hu, S.; Yang, J.; Xie, Y. Metallic few-layered VS$_2$ ultrathin nanosheets: high two-dimensional conductivity for in-plane supercapacitors. *J. Am. Chem. Soc.* **2011**, *133*, 17832−8.

(28) Wu, C.; Feng, F.; Xie, Y. Design of vanadium oxide structures with controllable electrical properties for energy applications. *Chem. Soc. Rev.* **2013**, *42*, 5157−83.

(29) Sun, Y.; Gao, S.; Lei, F.; Liu, J.; Liang, L.; Xie, Y. Atomically-thin non-layered cobalt oxide porous sheets for highly efficient oxygen-evolving electrocatalysts. *Chem. Sci.* **2014**, *5*, 3976−3982.

(30) Xie, Y.; Yu, Y.; Gong, X.; Guo, Y.; Guo, Y.; Wang, Y.; Lu, G. Effect of the crystal plane figure on the catalytic performance of MnO$_2$ for the total oxidation of propane. *CrystEngComm* **2015**, *17*, 3005−3014.

(31) Zhang, S.; Liu, S.; Zhu, X.; Yang, Y.; Hu, W.; Zhao, H.; Qu, R.; Zheng, C.; Gao, X. Low temperature catalytic oxidation of propane over cobalt-cerium spinel oxides catalysts. *Appl. Surf. Sci.* **2019**, *479*, 1132−1140.

(32) Xie, Y.; Guo, Y.; Guo, Y.; Wang, L.; Zhan, W.; Wang, Y.; Gong, X.; Lu, G. A highly effective Ni-modified MnO$_x$ catalyst for total oxidation of propane: the promotional role of nickel oxide. *RSC Adv.* **2016**, *6*, 50228−50237.

(33) Miniajluk, N.; Trawczyński, J.; Zawadzki, M. Properties and catalytic performance for propane combustion of LaMnO$_3$ prepared under microwave-assisted glycothermal conditions: Effect of solvent diols. *Appl. Catal. A: Gen.* **2017**, *531*, 119−128.

(34) Chai, G.; Zhang, W.; Liotta, L. F.; Li, M.; Guo, Y.; Giroir-Fendler, A. Total oxidation of propane over Co3O4-based catalysts: Elucidating the influence of Zr dopant. *Appl. Catal. B: Environ.* **2021**, *298*, 120606.

(35) Cai, T.; Deng, W.; Xu, P.; Yuan, J.; Liu, Z.; Zhao, K.; Tong, Q.; He, D. Great activity enhancement of Co$_3$O$_4$/c-Al$_2$O$_3$ catalyst for propane combustion by structural modulation. *Chem. Eng. J.* **2020**, *395*, 125071.

(36) Tang, Z. Y.; Zhang, Z. L.; Wang, Y.; Glotzer, S. C.; Kotov, N. A. Self-assembly of CdTe nanocrystals into free-floating sheets. *Science* **2006**, *314*, 274−278.

(37) Wang, D.; Ma, X.; Wang, Y.; Wang, L.; Wang, Z.; Zheng, W.; He, X.; Li, J.; Peng, Q.; Li, Y. Shape control of CoO and LiCoO$_2$ nanocrystals. *Nano Res.* **2010**, *3*, 1−7.

(38) Itteboina, R.; Sau, T. K. Sol-gel synthesis and characterizations of morphology-controlled Co$_3$O$_4$ particles. *Mater. Today: Proceedings* **2019**, *9*, 458−467.

(39) Yan, Z.; Xu, Z.; Cheng, B.; Jiang, C. Co$_3$O$_4$ nanorod-supported Pt with enhanced performance for catalytic HCHO oxidation at room temperature. *Appl. Surf. Sci.* **2017**, *404*, 426−434.

(40) Lou, Y.; Ma, J.; Cao, X.; Wang, L.; Dai, Q.; Zhao, Z.; Cai, Y.; Zhan, W.; Guo, Y.; Hu, P.; Lu, G.; Guo, Y. Promoting Effects of In$_2$O$_3$ on Co$_3$O$_4$ for CO Oxidation: Tuning O$_2$ Activation and CO Adsorption Strength Simultaneously. *ACS Catal.* **2014**, *4*, 4143−4152.

(41) Liu, Q.; Wang, L. C.; Chen, M.; Cao, Y.; He, H.-Y.; Fan, K. N. Dry citrate-precursor synthesized nanocrystalline cobalt oxide as highly active catalyst for total oxidation of propane. *J. Catal.* **2009**, *263*, 104−113.

(42) Zhu, J.; Bai, L.; Sun, Y.; Zhang, X.; Li, Q.; Cao, B.; Yan, W.; Xie, Y. Topochemical transformation route to atomically thick Co$_3$O$_4$ nanosheets realizing enhanced lithium storage performance. *Nanoscale* **2013**, *5*, 5241−6.

(43) Zhang, Q.; Mo, S.; Chen, B.; Zhang, W.; Huang, C.; Ye, D. Hierarchical Co$_3$O$_4$ nanostructures in-situ grown on 3D nickel foam towards toluene oxidation. *Mol. Catal.* **2018**, *454*, 12−20.

(44) Wei, R.; Fang, M.; Dong, G.; Lan, C.; Shu, L.; Zhang, H.; Bu, X.; Ho, J. C. High-Index Faceted Porous Co$_3$O$_4$ Nanosheets with Oxygen Vacancies for Highly Efficient Water Oxidation. *ACS Appl. Mater. Interfaces* **2018**, *10*, 7079−7086.

(45) Wang, K.; Cao, Y.; Hu, J.; Li, Y.; Xie, J.; Jia, D. Solvent-Free Chemical Approach to Synthesize Various Morphological Co$_3$O$_4$ for CO Oxidation. *ACS Appl. Mater. Interfaces* **2017**, *9*, 16128−16137.

(46) Cai, Z.; Bi, Y.; Hu, E.; Liu, W.; Dwarica, N.; Tian, Y.; Li, X.; Kuang, Y.; Li, Y.; Yang, X. Q.; Wang, H.; Sun, X. Single-Crystalline Ultrathin Co$_3$O$_4$ Nanosheets with Massive Vacancy Defects for Enhanced Electrocatalysis. *Adv. Energy Mater.* **2018**, *8*, 1701694.

(47) Chen, X.; Liu, B.; Zhong, C.; Liu, Z.; Liu, J.; Ma, L.; Deng, Y.; Han, X.; Wu, T.; Hu, W.; Lu, J. Ultrathin Co$_3$O$_4$ Layers with Large Contact Area on Carbon Fibers as High-Performance Electrode for Flexible Zinc-Air Battery Integrated with Flexible Display. *Adv. Energy Mater.* **2017**, *7*, 1700779.

(48) Huang, J.; Chen, J.; Yao, T.; He, J.; Jiang, S.; Sun, Z.; Liu, Q.; Cheng, W.; Hu, F.; Jiang, Y.; Pan, Z.; Wei, S. CoOOH Nanosheets with High Mass Activity for Water Oxidation. *Angew. Chem.* **2015**, *127*, 8846−8851.

(49) Gao, S.; Sun, Z.; Liu, W.; Jiao, X.; Zu, X.; Hu, Q.; Sun, Y.; Yao, T.; Zhang, W.; Wei, S.; Xie, Y. Atomic layer confined vacancies for atomic-level insights into carbon dioxide electroreduction. *Nat. Commun.* **2017**, *8*, 14503.

(50) Banerjee, A. N.; Anitha, V. C.; Joo, S. W. Improved electrochemical properties of morphology-controlled titania/titanate nanostructures prepared by in-situ hydrothermal surface modification of self-source Ti substrate for high-performance supercapacitors. *Sci. Rep.* **2017**, *7*, 13227.

(51) Yan, C.; Zhu, Y.; Li, Y.; Fang, Z.; Peng, L.; Zhou, X.; Chen, G.; Yu, G. Local built-in electric field enabled in carbon-doped Co$_3$O$_4$ nanocrystals for superior lithium-ion storage. *Adv. Funct. Mater.* **2018**, *28*, 1705951.

(52) Li, R.; Huang, Y.; Zhu, D. D.; Ho, W. K.; Cao, J. J.; Lee, S. C. Improved Oxygen Activation over a Carbon/Co$_3$O$_4$ Nanocomposite for Efficient Catalytic Oxidation of Formaldehyde at Room Temperature. *Environ. Sci. Technol.* **2021**, *55*, 4054−4063.

(53) Tian, M.; Jian, Y.; Ma, M.; He, C.; Chen, C.; Liu, C.; Shi, J. W. Rational design of CrO$_x$/LaSrMnCoO$_6$ composite catalysts with superior chlorine tolerance and stability for 1,2-dichloroethane deep destruction. *Appl. Catal. A-Gen.* **2019**, *570*, 62−72.

(54) Jian, Y.; Ma, M.; Chen, C.; Liu, C.; Yu, Y.; Hao, Z.; He, C. Tuning the micromorphology and exposed facets of MnO$_x$ promotes methyl ethyl ketone low-temperature abatement: boosting oxygen activation and electron transmission. *Catal. Sci. Technol.* **2018**, *8*, 3863−3875.

(55) Hu, Z.; Liu, X.; Meng, D.; Guo, Y.; Guo, Y.; Lu, G. Effect of Ceria Crystal Plane on the Physicochemical and Catalytic Properties of Pd/Ceria for CO and Propane Oxidation. *ACS Catal.* **2016**, *6*, 2265−2279.

(56) Wang, Z.; Huang, Z.; Brosnahan, J. T.; Zhang, S.; Guo, Y.; Guo, Y.; Wang, L.; Wang, Y.; Zhan, W. Ru/CeO$_2$ Catalyst with Optimized CeO$_2$ Support Morphology and Surface Facets for Propane Combustion. *Environ. Sci. Technol.* **2019**, *53*, 5349−5358.

(57) Pradhan, S.; Bartley, J. K.; Bethell, D.; Carley, A. F.; Conte, M.; Golunski, S.; House, M. P.; Jenkins, R. L.; Lloyd, R.; Hutchings, G. J. Non-lattice surface oxygen species implicated in the catalytic partial oxidation of decane to oxygenated aromatics. *Nat. Chem.* **2012**, *4*, 134−9.

(58) Zhang, J.; Liu, X.; Blume, R.; Zhang, A. H.; Schlogl, R.; Su, D. S. Surface-modified carbon nanotubes catalyze oxidative dehydrogenation of n-butane. *Science* **2008**, *322*, 73−77.

(59) Ren, Z.; Wu, Z.; Song, W.; Xiao, W.; Guo, Y.; Ding, J.; Suib, S. L.; Gao, P. X. Low temperature propane oxidation over Co$_3$O$_4$ based nano-array catalysts: Ni dopant effect, reaction mechanism and structural stability. *Appl. Catal., B* **2016**, *180*, 150−160.

(60) Li, X.; Li, X.; Zeng, X.; Zhu, T. Correlation between the physicochemical properties and catalytic performances of micro/mesoporous CoCeO mixed oxides for propane combustion. *Appl. Catal. A-Gen.* **2019**, *572*, 61−70.

(61) Hasan, M. A.; Zaki, M. I.; Pasupulety, L. IR investigation of the oxidation of propane and likely C(3) and C(2) products over group IVB metal oxide catalysts. *J. Phys. Chem. B* **2002**, *106*, 12747−12756.

(62) Chen, X. M.; Yang, X. F.; Zhu, A. M.; Fan, H. Y.; Wang, X. K.; Xin, Q.; Zhou, X. R.; Shi, C. In situ DRIFTS study on the partial oxidation of ethylene over Co-ZSM-5 catalyst. *Catal. Commun.* **2009**, *10*, 428−432.

(63) Zhang, F.; Zhang, S.; Guan, N.; Schreier, E.; Richter, M.; Eckelt, R.; Fricke, R. NO-SCR with propane and propene on Co-based alumina catalysts prepared by co-precipitation. *Appl. Catal., B* **2007**, *73*, 209−219.

(64) Zou, X.; Rui, Z.; Song, S.; Ji, H. Enhanced methane combustion performance over NiAl$_2$O$_4$-interface-promoted Pd/γ-Al$_2$O$_3$. *J. Catal.* **2016**, *338*, 192−201.

(65) Klisińska, A.; Haras, A.; Samson, K.; Witko, M.; Grzybowska, B. Effect of additives on properties of vanadia-based catalysts for oxidative dehydrogenation of propane. *J. Mol. Catal. A-Chem.* **2004**, *210*, 87−92.

(66) Miniajluk, N.; Trawczyński, J.; Zawadzki, M. Properties and catalytic performance for propane combustion of LaMnO$_3$ prepared under microwave-assisted glycothermal conditions: Effect of solvent diols. *Appl. Catal. A-Gen.* **2017**, *531*, 119−128.